PROCEEDINGS OF SPIE

SPIEDigitalLibrary.org/conference-proceedings-of-spie

Spatial-impulse-response-dependent back-projection using the non-stationary convolution in optoacoustic mesoscopy

Tong Lu, Yihan Wang, Feng Gao, Huijuan Zhao, Vasilis Ntziachristos, et al.

Tong Lu, Yihan Wang, Feng Gao, Huijuan Zhao, Vasilis Ntziachristos, Jiao Li, "Spatial-impulse-response-dependent back-projection using the non-stationary convolution in optoacoustic mesoscopy," Proc. SPIE 10494, Photons Plus Ultrasound: Imaging and Sensing 2018, 104943R (19 February 2018); doi: 10.1117/12.2290000



Event: SPIE BiOS, 2018, San Francisco, California, United States

Spatial-impulse-response-dependent back-projection using the nonstationary convolution in photoacoustic mesoscopy

Tong Lu^a, Yihan Wang^a, Feng Gao^{a,b}, Huijuan Zhao^{a,b}, Vasilis Ntziachristos^{c, d}, Jiao Li^{a,b,*}
^aSchool of Precision Instruments and Optoelectronics Engineering, Tianjin University, Tianjin 300072, China; ^bTianjin Key Laboratory of Biomedical Detecting Techniques and Instruments, Tianjin 300072, China; ^cInstitute for Biological and Medical Imaging, Helmholtz Zentrum München, Deutsches Forschungszentrum für Gesundheit und Umwelt (GmbH), IngolstädterLandstr.,85764 Neuherberg, Germany; ^dChair for Biological Imaging, Technische Universität München (TUM), Ismaningerstr. 22, 81675 München, Germany

*jiaoli@tju.edu.cn

ABSTRACT

Photoacoustic mesoscopy (PAMe), offering high-resolution (sub-100- μ m) and high optical contrast imaging at the depth of 1-10 mm, generally obtains massive collection data using a high-frequency focused ultrasonic transducer. The spatial impulse response (SIR) of this focused transducer causes the distortion of measured signals in both duration and amplitude. Thus, the reconstruction method considering the SIR needs to be investigated in the computation-economic way for PAMe. Here, we present a modified back-projection algorithm, by introducing a SIR-dependent calibration process using a non-stationary convolution method. The proposed method is performed on numerical simulations and phantom experiments of microspheres with diameter of both 50 μ m and 100 μ m, and the improvement of image fidelity of this method is proved to be evident by methodology parameters. The results demonstrate that, the images reconstructed when the SIR of transducer is accounted for have higher contrast-to-noise ratio and more reasonable spatial resolution, compared to the common back-projection algorithm.

Keywords: Photoacoustic mesoscopy, reconstruction algorithms, spatial impulse response, non-stationary convolution

1. INTRODUCTION

Photoacoustic mesoscopy (PAMe), also known as acoustic resolution photoacoustic microscopy (AR-PAM), is a rapidly emerging imaging modality that has great potential for a wide range of biomedical imaging applications ^[1-3]. PAMe is a hybrid imaging modality that synergistically combines the advantages of optical imaging and ultrasound imaging, offering high optical contrast image at deeper depths of multiple millimeters with resolutions well below 100µm. This technology is suitable for *in vivo* tumor experiment of small animal model and preliminary clinical study mostly focused on dermatology to explore the fine structural and functional information of the target ^[4-6]. In PAMe, the sample absorbs the energy and generates ultrasound waves. The propagating ultrasound waves can be detected by the surrounding sphere-focused ultrasonic detector as the photoacoustic signals and used to reconstruct photoacoustic images mapping the distribution of absorbed light energy in the biological sample.

Several reconstruction algorithms have been reported to achieve the reconstructed images, such as time-reversal algorithm, model-base method and back-projection methods ^[7-9]. Most photoacoustic reconstruction methods assume that the employed transducer can be viewed as the point-like transducer in the beginning, which is reasonable when the size of transducer is small or the source-detector distance is relatively large. However, it has been proved that the characteristics of transducer can make an influence on the imaging performance. Therefore, the impulse response of transducer has been investigated, including the electrical impulse response (EIR) and spatial impulse response (SIR) ^[10,11]. In the forward propagation process, the spatially propagated photoacoustic signal may arrive at different points on the detector surface at different times, thus the duration of the photoacoustic signal received by the detector is longer than the original photoacoustic signal. In addition, the intensity of the response of the focused ultrasound detector to the signal is different, related to the frequency of signals and spatial locations. Thus, the photoacoustic signals received by the detector are distorted to varying degrees. The above effect is the SIR of the detector, which depends on the shape of

Photons Plus Ultrasound: Imaging and Sensing 2018, edited by Alexander A. Oraevsky, Lihong V. Wang, Proc. of SPIE Vol. 10494, 104943R · © 2018 SPIE · CCC code: 1605-7422/18/\$18 · doi: 10.1117/12.2290000

the detector and the position of the signal source. Then, the signal output by the ultrasonic detector is the convolution of the distorted photoacoustic signal and the EIR which is acted as a band-pass filter around the center frequency of the detector and related to the piezoelectric characteristics.

The EIR can be obtained via experiment measurements or theoretical analyses [10], thus the influence of EIR can be removed by the deconvolution with received signals commonly used in many algorithms. The SIR has been matured in model-base algorithm requiring the detected photoacoustic signal and the impulse response of the detector to carry out inverse convolution [12,13]. However, in terms of large datasets in PAMe, the back-projection algorithm is more suitable for fast and efficient computation. In back-projection, the maximum value of SIR is usually chosen as the weighted matrix during reconstruction [14,15], which cannot fully reflect the effect of SIR. For the necessary close distance between transducer and object to effectively receive the high-frequency signals in PAMe, the characteristics including the shape of transducer are extremely needed to be considered. In this paper, the method of spatial-impulse-response-dependent back-projection is carried out to integrate the SIR in back-projection algorithm. The performance of the proposed method is validated by both simulation results and experiment results.

2. METHODS

2.1 Theory of photoacoustic imaging

When the pulse laser is under the heat confinement and pressure confinement, the instantaneous initial sound pressure is $P_{\theta}(\mathbf{r},t) = p_{\theta}(\mathbf{r})\delta(t)$. The photoacoustic wave equation describing the generation and propagation of photoacoustic signals in lossless medium can be expressed as

$$\nabla^2 p(\mathbf{r}, t) - \frac{I}{c^2} \frac{\partial^2 p(\mathbf{r}, t)}{\partial t^2} = -\frac{p_{\theta}(\mathbf{r})}{c^2} \frac{\partial \delta(t)}{t}$$
(1)

where $p(\mathbf{r},t)$ is the photoacoustic signal at position \mathbf{r} and time t, c is the speed of sound in the medium and $p_{\theta}(\mathbf{r})$ is the initial pressure we need to obtain. There is a common back-projection algorithm [9] for the inversion of (1):

$$p_{0}(\mathbf{r}) = \frac{1}{\Omega_{0}} \int_{s} d\Omega \left[2p(\mathbf{r}_{S}, t) - 2t \frac{\partial p(\mathbf{r}_{S}, t)}{\partial t} \right]_{t = |\mathbf{r}_{S} - \mathbf{r}|/c}$$
(2)

where $d\Omega$ is the solid angle element and Ω_0 is the solid angle related to the whole surface S; \mathbf{r} is the reconstruction position; $p(\mathbf{r}_S, t)$ is the pressure received at different detecting position \mathbf{r}_S .

However, in practice, the photoacoustic signal $p(\mathbf{r},t)$ suffers the distortion by the EIR and SIR, which means the signal we measured is:

$$p_m(\mathbf{r},t) = p(\mathbf{r},t) * h_s(\mathbf{r},t) * h_e(t)$$
(3)

where $h_{c}(\mathbf{r},t)$ is the SIR, $h_{e}(t)$ is the EIR and $p_{m}(\mathbf{r},t)$ is the measured signal.

2.2 Theory of time-space filter

In this paper, we focuses on the significance of SIR, so the signals are already deconvoluted with the EIR obtained by experimental measurement. When the photoacoustic signal is detected by an ultrasonic transducer with a finite surface s, the different points \mathbf{r}_d on the surface of the detector will intercept the photoacoustic signal at different times. Thus, the SIR can be mathematically expressed as the spatial mean of the photoacoustic field obtained by the detector surface:

$$h_{s}(\mathbf{r},t) = \int_{s} \frac{\mathcal{S}(t - \frac{|\mathbf{r}_{d} - \mathbf{r}|}{c})}{|\mathbf{r}_{d} - \mathbf{r}|} d\mathbf{r}_{d}$$
(4)

The exact solution of SIR for slightly sphere-focused transducers is provided and proved in ^[16]. By setting the parameters such as sampling frequency, diameter and focus of transducer, the corresponding solution of SIR can be obtained in the well-setting region of interest (ROI).

Since the SIR is mutative at different positions, we develop a spatiotemporal filter of focusing ultrasonic detector to establish the spatial-impulse-response-dependent back-projection reconstruction method. Combined with the nonstationary convolution method in seismology [17] where the filter changes with time, we expand this definition as the SIR changes with position which can be expressed mathematically as

$$p_{\theta}(\mathbf{r}) = p_{\theta,\mathbf{r}}(t) = \int_{-\infty}^{\infty} h_{s,\mathbf{r}}(t,t-\tau) p_{s}(\tau) d\tau$$
 (5)

where $\mathbf{r} = ct$ and one position corresponds to one time point, $p_s(\tau)$ is the detected signal after deconvolution with EIR. Equation (5) indicates that for each signal $p_s(\tau)$, the spatiotemporal filter is unique for each reconstruction position. In practice, the discrete version of (5) is often used in the reconstruction process:

$$\begin{bmatrix} p_0(\mathbf{r}_I) \\ \vdots \\ p_0(\mathbf{r}_M) \end{bmatrix} = \begin{bmatrix} p_{0,\mathbf{r}_I}(t_I) \\ \vdots \\ p_{0,\mathbf{r}_M}(t_M) \end{bmatrix} = \begin{bmatrix} h_{\mathbf{r}_I}(t_I,t_I-\tau_I) & \cdots & h_{\mathbf{r}_I}(t_I,t_I-\tau_N) \\ \vdots & & \vdots \\ h_{\mathbf{r}_M}(t_M,t_M-\tau_I) & \cdots & h_{\mathbf{r}_M}(t_M,t_M-\tau_N) \end{bmatrix} \begin{bmatrix} p_s(\tau_I) \\ \vdots \\ p_s(\tau_N) \end{bmatrix}$$
(6)

where M is the total number of reconstruction positions, N is the time series of photoacoustic signal. The impulse response is independent among each row. h is an M×N convolution matrix, and usually M>>N, thus the grid density can be guaranteed to reconstruct the high quality images. In the following, we refer to the proposed algorithm as SIRBP method.

3. RESULTS

The PAMe system components are shown in Figure 1, and the basic settings are described in the detail in Ref. 18. A tunable optical parametric oscillator laser (Phocus II, Opotek Inc., Carlsbad, California) is the laser source, providing the short-pulsed laser light with a repetition rate of 10 Hz and sub-10 ns pulse duration. The beam is guided into a custom-made 640-fiber bundles then delivered into four arms. A sphere-focused ultrasound detector with the center frequency of 15 MHz is mounted on two motorized precision stages: a translation stage and a rotation stage (M-605.2DD and M-062.PD, Physik Instrumente, GmbH, Germany). The stages are selected to format the translate-rotate scanner, which enables an accurate scanning mode during tomographic measurements. The diameter of the detector is 6 mm and focus is 19.8 mm. The signals are acquired at a rate of 125 MS/s. Each detected signal is first amplified by the amplifier and then digitized via a data acquisition (DAQ) card with the high sampling rate based on the frequency band of the used detector. Photoacoustic signals measured at multiple positions around the ROI are finally stored by the computer controlling system, used to reconstruct the absorbed energy distribution in the biological tissues.

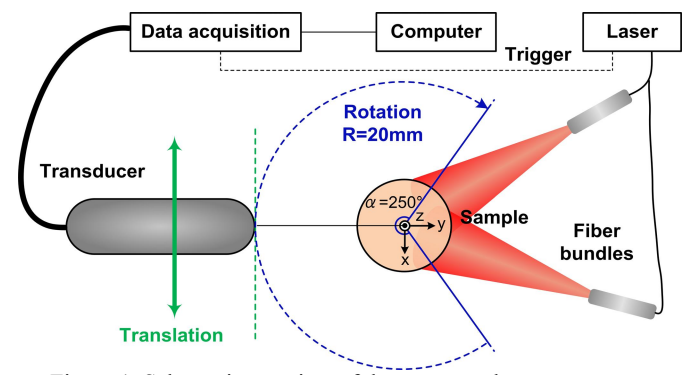


Figure 1. Schematic top view of the set-up and scan geometry.

The results obtained with the SIRBP method are compared with common back projection (BP) and weighted back projection (WBP) reconstructions. The signals used in all the three methods are after the devolution with EIR. In this paper, the weighted matrix in WBP method is the maximum value of SIR in the ROI.

3.1 Simulation results

To access the validity of SIRBP for PAMe imaging, a numerical phantom with absorbers of 60 μ m, 100 μ m, 120 μ m and 200 μ m diameter is investigated. The forward simulated data are generated by a simulation toolbox named K-Wave [19]. For simulation, the number of projections is 3600 and the number of time instants is 1500, with a sampling

frequency of 100 MHz. In view of the scanning density, we choose 180 positions for rotary stage in total, with a 2 deg angular step. At each rotation position, the detector moves linearly in step of 500 μ m, with a total of 20 positions. The rotation radius is 10 mm and the diameter of detector is 3.4 mm, which are scaled down in equal proportion according to the transducer used in practice. The reconstructed region is 7mm \times 7mm, fully covering the target. The speed of sound is set to be 1500 m/s. The center of phantom is almost overlapped with the focus of transducer.

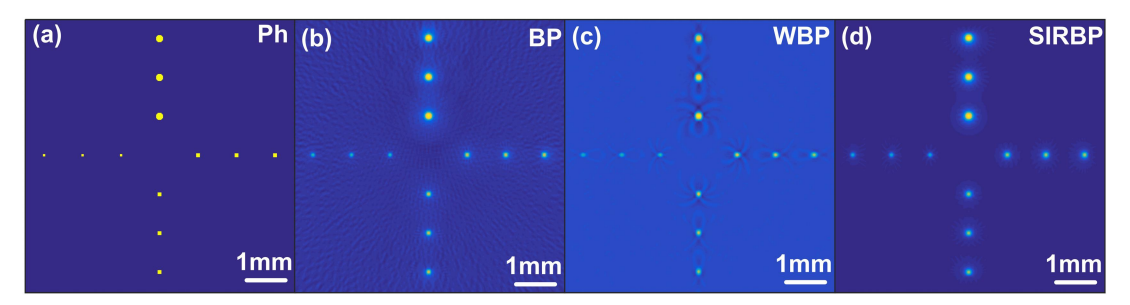


Figure 2. (Simulation) Image reconstructions of different sizes of absorbing spheres. (a) Numerical phantom (Ph). Reconstructions performed with (b) the BP method, (c) the WBP method and (d) the SIRBP method. The sizes of absorbers are: 60 μm, 100 μm, 120 μm and 200 μm diameter.

The phantom photo and the reconstructed images obtained by the three algorithms are shown in Figure 2. The BP result presents clear artifacts, resulting from the heterogeneous sensitivity field of sphere-focused detector. The WBP and SIRBP results are cleaner, and the background in SIRBP result is darker which means a better suppression for background noise. In order to compare the three method explicitly, we calculate the full width at half maximum (FWHM) and contrast-to-noise ratio (CNR) of four absorbers, shown in Figure 3. Both the FWHM and CNR of different sizes absorbers are the average of each three absorbers of the same size. The sizes of 120 µm and 200 µm absorbers are relatively smaller in the WBP result, but the accuracy of reconstruction cannot be matched to the original image. From an overall perspective, the red line in Figure 3(a) is closer to the standard black line, which means the imaging improvement by use of SIRBP method. In Figure 3(b), the better contrast in SIRBP image is noticeable for all four sizes absorbers.

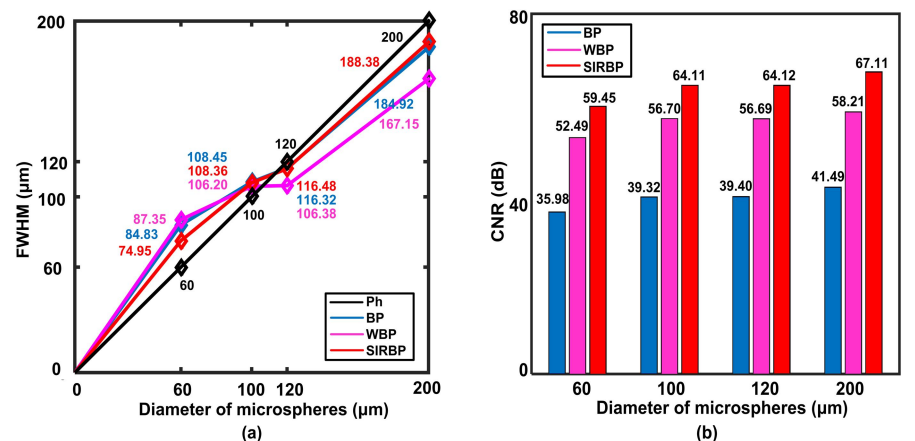


Figure 3. (a) FWHM of four different sizes microspheres. (b) CNR of four different sizes microspheres.

Furthermore, the peak signal-to-noise ratio (PSNR) and the distance (d) are chosen to quantitatively evaluate the reconstruction quality of three algorithms with the original image as the standard. The PSNR is defined as

$$PSNR(dB) = 10 \log_{10} \left(N_x N_y / \sum_{i=1}^{N_x} \sum_{j=1}^{N_y} (f_{i,j} - r_{i,j})^2 \right)$$
 (7)

where f is the gray value of the reconstructed image and r is the gray value of the phantom. The size of the image is $N_x \times N_y$. The distance between the reconstructed image and original phantom image can be expressed as

$$d = \sqrt{\left(\sum_{i=1}^{N_x} \sum_{j=1}^{N_y} \left(f_{i,j} - r_{i,j}\right)^2 / \sum_{i=1}^{N_x} \sum_{j=1}^{N_y} r_{i,j}^2\right)}$$
(8)

The calculated PSNR for the BP method, WBP method and SIRBP method are 26.6, 20.6, 30.9, respectively. It can be derived that the SIRBP algorithm is able to obtain the reconstructed images with high fidelity compared with other algorithms in the PAMe. Besides, the distance of the BP method, WBP method and SIRBP method are 0.89, 1.77, 0.55, which means the SIRBP result is closest to the original phantom image.

3.2 Experiment results

Two agar phantoms are used in the experiment, with 50 µm and 100 µm diameter black microspheres randomly dispersed in agar gel, respectively. The reconstructed results of these two kinds of microspheres in ROI are presented in Figure 4 and Figure 6. The scanning radius of transducer is set to be 20 mm, approximately equal to the focal length. There are 3690 projections (180 angular positions and a translation step of 0.5 mm) and 2048 time instants for all the three reconstruction methods. The distribution of microspheres is clearly recognized on all three reconstructed images. By using a weighted matrix in WBP algorithm, the homogeneity of background is enhanced but the magnitude of background is also increased. Comparing the SIRBP with BP reconstructions, an effective inhibition on the background noise can be observed.

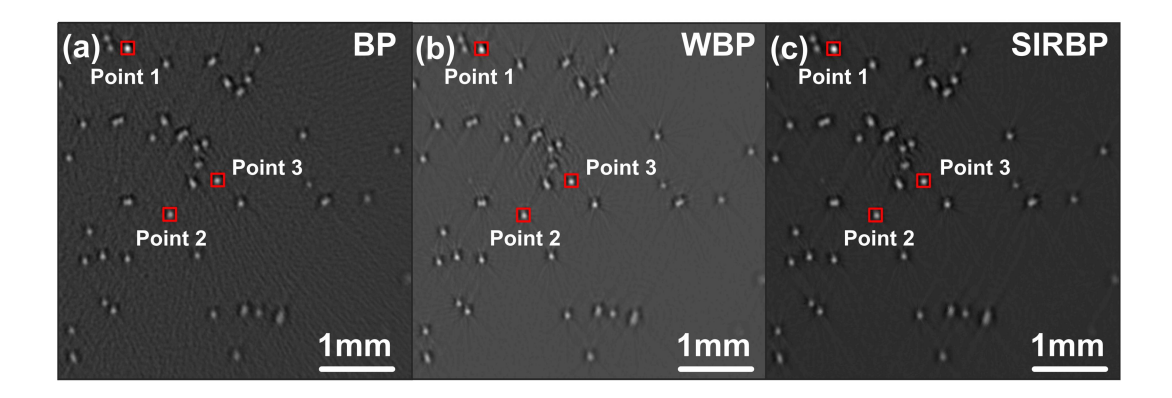


Figure 4. (Experiment) Image reconstructions of 50 µm diameter microspheres with (a) the BP method, (b) the WBP method and (c) the SIRBP method.

There are three microspheres selected randomly to specifically analyze the quality of the three reconstruction results. From the profiles in Figure 5, the WBP results are generally improved in terms of resolution compared with BP results. However, the magnitude of some value is at a loss. On the contrary, the improvement of reconstruction combing SIR is evident. After deconvolution with SIR, the effect of sidelobes is reduced, as well as the noise.

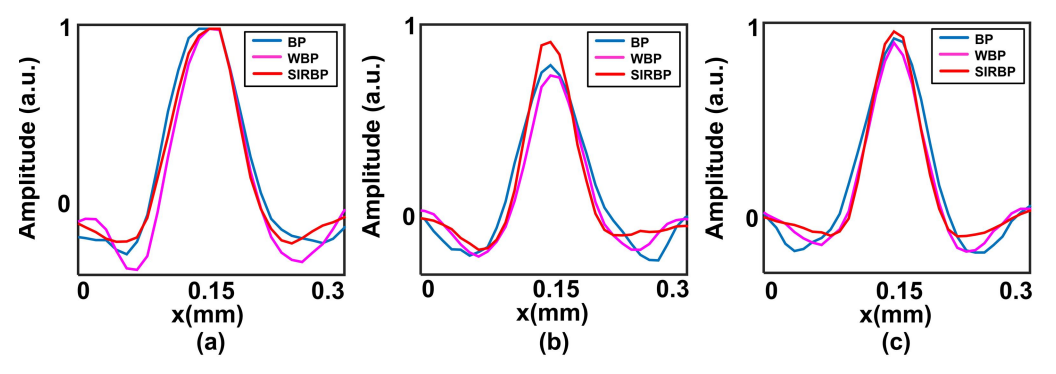


Figure 5. Profiles of three randomly selected microspheres along x-axis. (a) Point 1, (b) Point 2, and (c) Point 3.

The reconstructed methods are also performed on the 100 µm diameter black microspheres as further evidence. We employ 2970 projections (180 angular positions and a translation step of 0.6 mm) since the size of these microspheres is larger. Figure 6 shows the reconstructed results with BP, WBP and SIRBP methods. At a whole, the microspheres in SIRBP is brightest attributed to the high CNR, and the background is most uniform. From the profiles of two adjacent microspheres marked with red dashed lines, Figure 6(d) shows that the amplitude of signal may be decreased in WBP and SIRBP, but the resolution is maintained and the noise is reduced by use of SIRBP algorithm.

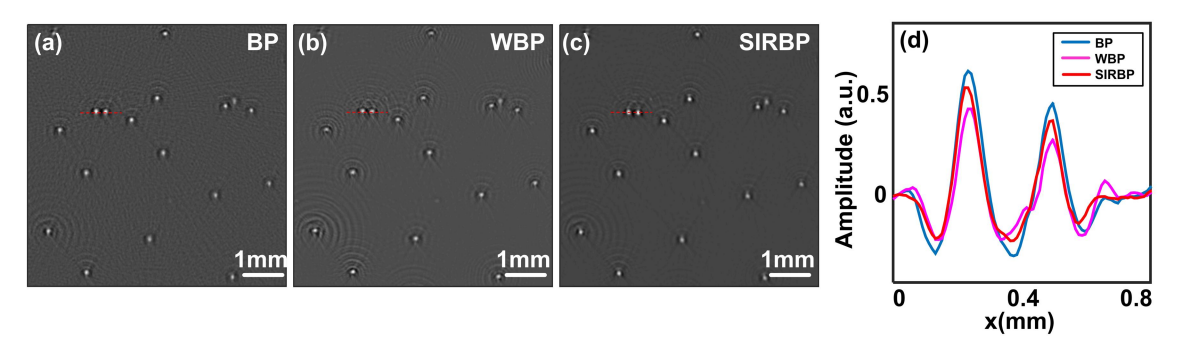


Figure 6. (Experiment) Image reconstructions of 100 µm diameter microspheres with (a) the BP method, (b) the WBP method and (c) the SIRBP method. (d) Profiles along the red dash lines marked in (a), (b) and (c).

4. CONCLUSIONS

As the mesoscopic scale of photoacoustic imaging, the large datasets and the impulse response of the used transducer are needed for reconstructing high quality and fidelity photoacoustic images. In this work, we introduced a spatial-impulse-response-dependent back-projection reconstruction algorithm considering the SIR for sphere focused transducer. By testing the performance of the proposed algorithm through simulation and phantom experiments, we proved that the method can improve the image quality and fidelity compared with the BP and WBP methods for several different sizes microspheres. The noise can be suppressed and the higher CNR is clearly observed. As a consequence, the proposed algorithm can incorporate the SIR of transducer and manage the large datasets of PAMe, which will be a major improvement for PAMe imaging.

ACKNOWLEDGEMENTS

The authors acknowledge the funding supports from the National Natural Science Foundation of China (81771880, 81401453, 81371602, 61475115, 61475116, 61575140, 81571723, 81671728,), and Tianjin Municipal Government of China (15JCZDJC31800, 15JCQNJC14500, 16JCZDJC31200, 17JCZDJC32700, 17JCQNJC12700).

REFERENCES

- [1] Taruttis, A., van Dam, G. M., Ntziachristos, V., "Mesoscopic and macroscopic optoacoustic imaging of cancer, "Cancer Research, 75(8), 1548-1559 (2015).
- [2] Chekkoury, A., Gateau, J., Driessen, W., et al., "Optical mesoscopy without the scatter: broadband multispectral optoacoustic mesoscopy," Biomedical Optics Express, 6(9),3134-3148 (2015).
- [3] Ntziachristos, V., "Going deeper than microscopy: the optical imaging frontier in biology, " Nature Methods, 7(8), 603-614 (2010).
- [4] Schwarz, M., Buehler, A., Aguirre, J., et al., "Three-dimensional multispectral optoacoustic mesoscopy reveals melanin and blood oxygenation in human skin in vivo," Journal of Biophotonics, 9(1-2),55-60 (2016).
- [5] Aguirre, J., Schwarz, M., Soliman, D., et al., "Broadband mesoscopic optoacoustic tomography reveals skin layers," Optics Letters, 39(21),6297-6300 (2014).
- [6] Schwarz, M., Omar, M., Buehler, A., et al., "Implications of ultrasound frequency in optoacoustic mesoscopy of the skin," IEEE Trans Med Imaging, 34(2), 672-677 (2015).

- [7] Treeby, B. E., Zhang, E. Z., Cox, B. T., "Photoacoustic tomography in absorbing acoustic media using time reversal, "Inverse Problems, 26157(26), 115003-115020 (2010).
- [8] Dean-Ben, X. L., Ntziachristos, V., Razansky, D., "Acceleration of Optoacoustic Model-Based Reconstruction Using Angular Image Discretization," IEEE Transactions on Medical Imaging, 31(5), 1154-1162 (2012).
- [9] Xu, M., Wang, L. V., "Universal back-projection algorithm for photoacoustic computed tomography," Physical review. E, Statistical, nonlinear, and soft matter physics, 71(2), 016706 (2005).
- [10] Wang, K., Ermilov, S. A., Su, R., et al., "An imaging model incorporating ultrasonic transducer properties for three-dimensional optoacoustic tomography.," IEEE Transactions on Medical Imaging, 30(2), 203-214 (2011).
- [11] Caballero, M. A. A., Rosenthal A, Buehler A, et al., "Optoacoustic determination of spatio- temporal responses of ultrasound sensors," IEEE Transactions on Ultrasonics Ferroelectrics & Frequency Control, 60(6),1234-1244 (2013).
- [12] Rosenthal, A., Ntziachristos, V., Razansky, D., "Model-based optoacoustic inversion with arbitrary-shape detectors," Medical Physics, 38(7), 4285-4295 (2011).
- [13] Ding, L., Dean-Ben, X. L., Razansky, D., "Efficient 3-D Model-Based Reconstruction Scheme for Arbitrary Optoacoustic Acquisition Geometries," IEEE Transactions on Medical Imaging, 36(9),1858-1867 (2017).
- [14] Li, Z., Li, Y., Guo, Z., et al., "Photoacoustic microscopy in vivo using synthetic-aperture focusing technique combined with three-dimensional deconvolution," Optics Express, 25(2),1421-1434 (2017).
- [15] Turner, J., Estrada, H., Kneipp, M., et al., "Improved optoacoustic microscopy through three-dimensional spatial impulse response synthetic aperture focusing technique," Optics Letters, 39(12),3390-3393 (2014).
- [16] Arditi, M., Foster, F. S., Hunt, J. W., "Transient fields of concave annular arrays," Ultrasonic Imaging, 3(1), 37-61 (1981).
- [17] Margrave, G. F., Lamoureux, M. P., Henley, D. C., "Gabor deconvolution: Estimating reflectivity by nonstationary deconvolution of seismic data, "Geophysics, 76(3), 15-30 (2011).
- [18] Gateau, J., Chekkoury, A., Ntziachristos, V., "High-resolution optoacoustic mesoscopy with a 24 MHz multidetector translate-rotate scanner," Journal of Biomedical Optics, 18(10), 106005 (2013).
- [19] Treeby, B. E., Cox, B. T., "k-Wave: MATLAB toolbox for the simulation and reconstruction of photoacoustic wave fields," Journal of Biomedical Optics, 15(2), 021314 (2010).